Adaptive Speed Control of PMSM Drive System Based a New Sliding-Mode Reaching Law

Abdul Khalique Junejo, Wei Xu, *Senior Member, IEEE*, Chaoxu Mu, *Senior Member, IEEE*, Moustafa Magdi Ismail, and Yi Liu, *Member, IEEE*

***Abstract*—In order to enhance the speed control performance of the permanent magnet synchronous motor (PMSM) with internal and external disturbances, a new adaptive terminal sliding mode reaching law (ATSMRL) is proposed with continuous fast terminal sliding mode control (CFTSMC). Firstly, the ATSMRL is presented with the aim of reducing the input control efforts, which can dynamically adopt all positive aspects in terms of the finite time convergence, high tracking precision, and reduction of the chattering in the control input of the system. Secondly, an extended sliding mode disturbance observer (ESMDO) is designed to estimate the total disturbances of the system, and then the estimated disturbance has been brought for the feed-forward compensation technique, which would enhance the disturbance rejection ability of the system. Afterwards, the close loop stability is validated by the Lyapunov function. Finally the comprehensive numerical and experimental analyses have been carried out to demonstrate the superiority of the ATSMRL method than those of conventional exponential sliding mode reaching law (ESMRL) and terminal sliding mode reaching law (TSMRL).**

***Index Terms*—Adaptive terminal sliding mode reaching law (ATSMRL), continuous fast terminal sliding mode control (CFTSMC), extended sliding mode disturbance observer (ESMDO), Lyapunov function, permanent magnet synchronous motor (PMSM), terminal sliding mode reaching law (TSMRL).**

I. Introduction

Permanent magnet synchronous motors (PMSMs) are simple in structure with high power density and high efficiency, which are widely used in the field of electric vehicles (EVs), robotics, computer numerical control (CNC) machines, aerospace, pumps and other fields of engineering [1]. PMSMs are multivariable with strong coupling and have the disturbances and uncertainties, e.g., load disturbances, parameter mismatch, friction, and unmolded dynamics.

If the linear control algorithm such as proportional integral (PI) controller is implemented in drive system, the control precision range would be limited to certain limit. At same time the PI controller depending on the system parameters, which means that the PI control methods are sensitive to the system model accuracy, which is highly susceptible to external disturbances and internal parameter mismatch. Therefore, it is essential to control aforementioned variations, but it is not easy to limit these disturbances by employing the linear algorithms, like PI controllers [2]. In order to overcome these problems, the nonlinear algorithms have been implemented in the field of servo systems for the realization of high performance control. The nonlinear algorithms include robust control [3], fuzzy control [4], sliding mode control (SMC) [5], disturbance rejection control [6], predictive control [7], [8], terminal sliding mode control (TSMC) [9]–[15], and so on. Among them, the SMC control algorithm has a priority in research area, because the SMC has not much requirement for the model accuracy, and has the strong robustness against all nonlinearities, e.g., external and internal disturbances. Till now, the SMC has been successfully applied in the field of servo systems [16].

However, it can be noted from the literature survey that the SMC has two parts, one is reaching law and the other is sliding mode surface. The reaching law helps the system states to reach the designed sliding mode surface, but it is difficult that the system states remain on the sliding surface with zero error [17]. The system states constantly traverse on both sides of sliding surface, which leads to the unavoidable chattering in the system. Therefore, the reduction of the chattering is key in the SMC. The reaching law design is important in the SMC, because the reaching law is directly related to the process of the system states to reach the sliding mode surface [18].

The chattering phenomenon is one inherent attribute of SMC, which is directly associated to the reaching law. The reaching law contains the switching function, which creates the chattering in the SMC. In order to guarantee the strong robustness against disturbances, the switching function gain must be set larger enough to compensate the system disturbances. However, it is difficult to know the exact upper bound of the disturbances. Due to larger switching gain, the reaching law would lead higher frequency chattering in the SMC. Thereof, it can be concluded that if the switching gain is decreased, then the system robustness

Manuscript received 23 October 2019; revised 25 January 2020; accepted 4 April 2020. Date of publication 12 April 2020; date of current version 20 July 2020. This work was supported in part by the National Natural Science Foundation of China under Grant 51877093, in part by the National Key Research and Development Program of China under Grant YS2018YFGH000299, and in part by the Key Technical Innovation Program of Hubei Province under Grant 2019AAA026. Recommended for publication by Associate Editor B. Mirafzal. *(Corresponding author: Wei Xu.)*

Abdul Khalique Junejo is with the State Key Laboratory of Advanced Electromagnetic Engineering and Technology, School of Electrical and Electronic Engineering, Huazhong University of Science and Technology, Wuhan 430074, China, and also with the Department of Electrical Engineering, Qaid-e-Awam University of Engineering, Science and Technology, Nawabshah, Sindh 67450, Pakistan (e-mail: ak.junejo@gmail.com).

Wei Xu, Moustafa Magdi Ismail, and Yi Liu are with the State Key Laboratory of Advanced Electromagnetic Engineering and Technology, School of Electrical and Electronic Engineering, Huazhong University of Science and Technology, Wuhan 430074, China (e-mail: weixu@hust.edu.cn; mostafa.ismaiel@minia.edu.eg; liuyi82@hust.edu.cn).

Chaoxu Mu is with the School of Electrical and Information Engineering, Tianjin University, Tianjin 300072, China (e-mail: cxmu@tju.edu.cn).

Digital Object Identifier 10.1109/TPEL.2020.2986893

against disturbances may be compromised. Thus, to alleviate this drawback of the SMC controller, more advanced reaching law and no-linear disturbances observer can be designed.

Traditionally, the exponential sliding mode reaching law (ESMRL) has an exponential term and proportional rate term. The procedure of this reaching law is to design the larger switching gain of proportional rate term so as to compensate the system disturbances. The larger switching gain leads the chattering phenomena in the system. The ESMRL can only guarantee the faster convergence, when the sliding states are near to the sliding mode surface [22]. Afterwards, the TSMRL has been designed to improve the system performance in terms of faster convergence, and the reduction of chattering [24]. In the design of TSMRL, the power rate term is added instead of the exponential term of ESMRL. The power rate term would make the sliding states faster when those would be far from the sliding mode surface. The TSMRL has better control performance than that of exponential reaching law in terms of convergence and chattering.

Therefore, in this article, one improved adaptive terminal sliding mode reaching law (ATSMRL) is proposed to increase the dynamic performance of the PMSM drive system. The proposed ATSMRL reaching law can improve the performance of reaching time and reduce the chattering effectively from the control system. Furthermore, one extended sliding mode disturbance observer (ESMDO) is designed to estimate the disturbances of the close loop system and enhance its disturbance rejection ability. The estimated disturbances are then considered for the feed-forward compensation with output of the speed loop.

This article is organized as follows. In Section II, it discusses the preliminaries with dynamic modeling of the PMSM, and general SMC design. In Section III, the CFTSMC with ATSMRL is designed for the speed regulation, and the ESMDO is designed for the estimation on total disturbances. Comprehensive experimental analyses have been made in Section IV, which demonstrate that the PMSM drive system has very strong robustness based on the proposed algorithm. Finally, the conclusion is summarized in Section V.

II. Preliminaries

A. Mathematical Model of the PMSM

The mathematical model of the PMSM under uncertainties and load disturbances with the motion and current dynamics can be expressed as [25]

$$\frac{d\omega}{dt} = \frac{G_t}{J} i_q - \frac{B}{J}\omega - \frac{n_p}{J} T_L \tag{1}$$

$$\frac{di_d}{dt} = -\frac{Rs}{L_s} i_d + n_p \omega i_q + \frac{u_d}{L_s} \tag{2}$$

$$\frac{di_q}{dt} = -\frac{Rs}{L_s} i_q + n_p \omega i_d - \frac{n_p \omega \psi_f}{L_s} + \frac{u_q}{L_s} \tag{3}$$

where $G_t = 2/3\ {n_p}^2 \psi_f$, n_p is the number of poles pairs, ψ_f the flux linkage, J the moment of inertia, B the viscous damping co-efficient, i_d, i_q u_d and u_q are the d and q-axis currents and voltages, separately, R_s and L_s the resistance and inductance of the stator, and T_L is the load torque of motor.

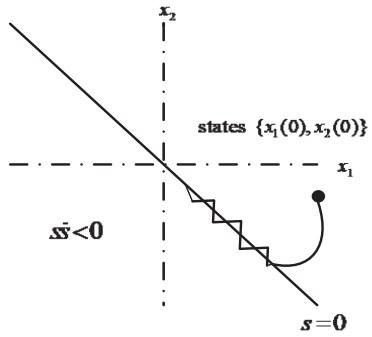

Fig. 1. Phase plane of SMC process.

B. SMC Design With TSMRL Reaching Law

The design of SMC controller has two stages, one is the sliding mode surface, and the other is the reaching law. However, the reaching law may produce the chattering phenomena in the system, which is very crucial in the SMC design. This problem motivates the researchers to introduce chattering free reaching laws. The chattering phenomena can be reduced effectively by implementing suitable techniques. In this section, the TSMRL is introduced to design the SMC, which must satisfy the following sliding mode reaching condition

$$s\dot{s} < 0 \tag{4}$$

where s is the sliding mode surface. Fig. 1 shows the phase plane of the SMC, which describes the reaching process of the system state on the designed sliding mode surface.

The second order nonlinear system is described as

$$\begin{cases} \dot{\chi}_1 = \chi_2 \\ \dot{\chi}_2 = h(\chi) + g(\chi) + b(\chi)u \end{cases} \tag{5}$$

where $\chi = [\chi_1, \chi_2]^T$ is the system state, u the control input and $g(\chi)$ the total disturbances of the system. The CFTSMC has been chosen as the sliding mode surface [12], which is described as

$$s = x_2 + \mu_1 |x_2|^{\sigma_1} \operatorname{sign}(x_2) + \mu_2 |x_1|^{\sigma_2} \operatorname{sign}(x_1) \tag{6}$$

where $\mu_1 > 0$, $\mu_2 > 0$, $0 < \sigma_1 < 2$, $\sigma_2 > \sigma_1$ and $\sigma_1 = \delta/\Theta$, both δ and θ are the odd positive number. In order to improve the whole system performance, it is desirable to reduce the chattering phenomena and enhance the finite convergence effectively. Thereof, the TSMRL can be designed according to the TSMRL [24], which must satisfy the reaching condition $s\dot{s} < 0$ with

$$\dot{s} = -\lambda_1(s) - \lambda_2 |s|^{\sigma_3} \operatorname{sign}(s) \tag{7}$$

where λ_1 and λ_2 are the two positive designed constants for the reaching phase $0 < \sigma_3 < 1$. Taking derivative of (6) and then

substituting in (7), it will get

$$-\lambda_1(s) - \lambda_2|s|^{\sigma_3}\,\mathrm{sign}(\vartheta) = \dot{x}_2 + \sigma_1\mu_1|x_2|^{\sigma_1-1}\dot{x}_2\,\mathrm{sign}\,(x_2) + \sigma_2\mu_2|x_1|^{\sigma_2-1}\,\mathrm{sign}\,(x_1)$$

$$0 = x_2 + \mu_1|x_2|^{\sigma_1}\,\mathrm{sign}\,(x_2) + \mu_2|x_1|^{\sigma_2}\,\mathrm{sign}\,(x_1) + \int \lambda_1(s) + \lambda_2|s|^{\sigma_3}\,\mathrm{sign}(\vartheta) \tag{8}$$

Substituting (5) into (8), the control input u can be described as

$$u = -\frac{1}{b(\chi)}\left[h(\chi) + g(\chi) + \mu_1|x_2|^{\sigma_1}\,\mathrm{sign}\,(x_2) + \mu_2|x_1|^{\sigma_2}\,\mathrm{sign}\,(x_1) + \int \lambda_1(s) + \lambda_2|s|^{\sigma_3}\,\mathrm{sign}(s)\right]. \tag{9}$$

In (9), there are two discontinuous terms $b^{-1}(\chi)$, and $\lambda_2|s|^{\sigma_3}\,\mathrm{sign}(s)$. The chattering phenomenon appears in the system due to these discontinuous terms. The chattering level is related to the switching gain value of λ_2. If λ_2 is larger, the chattering would be greater; while if λ_2 smaller, the chattering would be smaller [22]. The reaching time of the state variable can be derived by integrating (7) with respect to time, which can be written as

$$t = \frac{|s(0)|}{\lambda_1} + \frac{1}{\lambda_2(1+\sigma_3)}. \tag{10}$$

Eq. (10) shows that the reaching time of state is related to λ_1, λ_2, and σ_3. If the values of these switching gains are higher, then the reaching time would become smaller, but the chattering level would be higher [22]. Thereof, the optimal switching gain selection is very important in this work [2], [24].

C. Comparison of the ATSMRL, TSMRL, and Conventional ESMRL

Through numerical analyses, different reaching laws with CFTSMC are fully studied in this article. The ESMRL [22], TSMRL [24] and ATSMRL are compared in details. Main parameters are chosen as $h = -25\dot{x}$, $b = 133$, $g(t) = 10\sin(\pi t)$, and $x_a = \sin t$, respectively.

Fig. 2 shows the control input and the phase plane trajectory response of the system under ESMRL [22], TSMRL [24], and ATSMRL. Fig. 2(a) obviously shows that the proposed ATSMRL has better tracking, smaller chattering, and smaller steady state error than those of conventional reaching law ESMRL [22], and TSMRL [24]. Furthermore, Fig. 2(b) indicates that the ASMRL has faster convergence rate and smoother steady state process than those of the ESMRL [22] and TSMRL [24].

III. Design of Speed Controller for the PMSM Drive

A. Proposed ATSMRL

The TSMRL has the ability of alleviation in the chattering phenomena, and faster in the finite time convergence. The aforementioned characteristics of the TSMRL can be enhanced by designing ATSMRL based on the adaptive function, which can be described in Assumption 1.

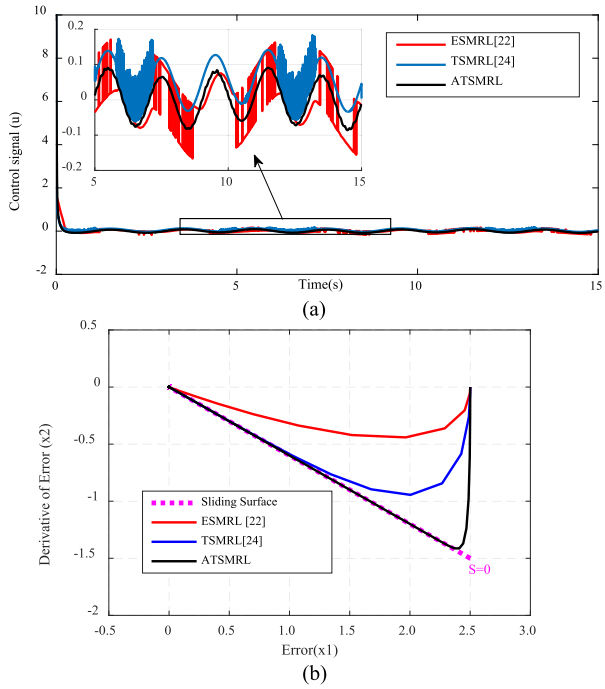

Fig. 2. Control performance of the system under ESMRL [22], TSMRL [24], and ATSMRL. (a) Input control u response. (b) Phase plane trajectory response.

Assumption 1: Let Ω_r be known as the reduction control amplitude gain, which can minimize the gain value of the controller and make the controller robust against disturbances of the system. The Ω_r must be positive, as defined by

$$\Omega_r = M_{\min}\Omega - H > 0 \tag{11}$$

where M and H are the positive constants and Ω is chosen as $\Omega = \frac{M}{H}$. Once the reduced control amplitude has been designed, the ATSMRL can be described as

$$\dot{s}_A = -\bar{\Omega}\,\mathrm{sign}\left\{s + \frac{\dot{s}\,|\dot{s}|}{2\Omega_r}\right\}. \tag{12}$$

The ATSMRL is based on TSMRL by using adaptive technique, and $\bar{\Omega}$ depends on the switching mechanism, then $\bar{\Omega} \in [-\Omega, \Omega]$, as described by

$$\bar{\Omega} = \begin{cases} \eta_1\,|s| - \eta_2\,|\dot{s}|\,; & \text{if } \bar{\Omega} > \frac{H}{M_{\min}} + \eta_3 \\ \eta_1\,|s| + \eta_2\,|\dot{s}|\,; & \text{if } \bar{\Omega} < \Omega \\ 0 & \text{otherwise} \end{cases} \tag{13}$$

where $\eta_1 > 0$, $\eta_2 > 0$, and $0 \le \eta_3 < \Omega$ are the constant arbitrarily gains to tune the optimal switching rate.

B. Design of Speed Controller

The speed controller should be designed in such a way that the tracking of the speed reference could be the actual speed under the load disturbances and uncertainties. To get this control target, the tracking error of the speed is described as

$$E = \omega_r - \omega. \tag{14}$$

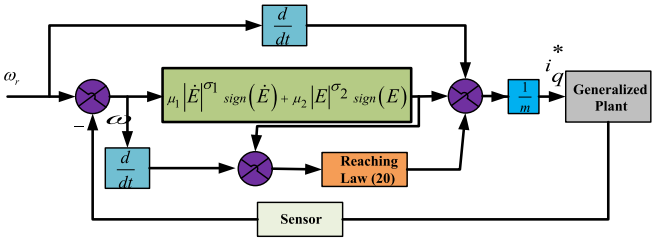

Fig. 3. Speed control block diagram of the PMSM drive under CFTSMC with ATSMRL method.

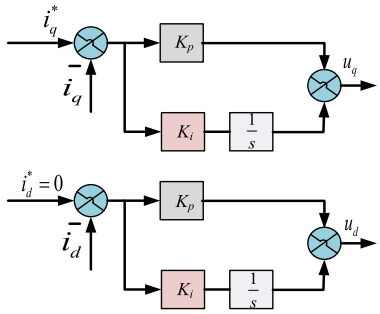

Fig. 4. PI controller block diagram for the current loops.

In this article, the speed ω is the control target of PMSM. Therefore, (1) can be rewritten as

$$\dot{\omega} = mi_q^* + D(t) \tag{15}$$

$$D(t) = -\frac{B}{J}\omega - \frac{T_L}{J} - \frac{G_t}{J}(i_q^* - i_q) \tag{16}$$

where $m = G_t/J$. Then, the CFTSMC has been chosen as the sliding mode surface for the speed loop [12], which is defined in (6). Taking the derivative of (14) and combining with (15), we will get

$$\dot{E} = \dot{\omega}_r - \dot{\omega} = \dot{\omega}_r - mi_q^* - D(t). \tag{17}$$

The SMC needs two parts, one is the sliding mode surface and the other is the reaching law. Thereof, the new ATSMRL is designed on the basis of (12).

Theorem 1: The speed error in (14) is selected as the state of the system, which would converge to the zero ($s = 0$), while the sliding surface in CFTSMC is preferred as (6) with the ATSMRL in (12). Therefore, the speed controller can be designed as

$$i_q^* = m^{-1}(H_{eq} + H_b) \tag{18}$$

$$H_{eq} = \dot{\omega}_r + \mu_1\left|\dot{E}\right|^{\sigma_1} \text{sign}\left(\dot{E}\right) + \mu_2|E|^{\sigma_2} \text{sign}\,(E) \tag{19}$$

$$H_b = \int_0^t -\bar{\Omega}\ \text{sign}\left\{s + \frac{\dot{s}\,|\dot{s}|}{2\Omega_r}\right\} dt. \tag{20}$$

The block diagram of the final control law is shown in Fig. 3.

C. Stability Analysis of the Speed Controller

The Lyapunov function is selected to check the stability of the speed loop. The Lyapnuov stability condition can be described as

$$\lim_{s\to 0}\dot{V} = \lim_{s\to 0} s\dot{s} \le 0. \tag{21}$$

By considering (6) and (12), (21) can be rewritten as

$$\dot{V} = s\dot{s}_A = s\left[-\bar{\Omega}\ \text{sign}\left\{s + \frac{\dot{s}\,|\dot{s}|}{2\Omega_r}\right\}\right]. \tag{22}$$

The conclusion can be drawn from (22), which is simplified as

$$\dot{V} = \left[-\bar{\Omega}\ \text{sign}\left\{s^2 + \frac{\dot{s}s\,|\dot{s}|}{2\Omega_r}\right\}\right]$$

$$\dot{V} = \left[-\bar{\Omega}\ \text{sign}\left\{2V + \frac{\dot{V}\,|\dot{s}|}{2\Omega_r}\right\}\right]. \tag{23}$$

In (23), $\bar{\Omega}$ and Ω_r are the constant gains, which are greater than zero, and $|\dot{s}|$ is the positive value. Therefore, the Lyapunov stability condition is fully satisfied. It can be concluded that the state variables of the system would converge to zero in the finite time.

D. Design of Current Controller

The structured controllers in series are employed for one speed loop and two current loops. Two PI controllers are adapted to the current loops, which can stabilize the current tracking errors of the *dq*-axis currents respectively. However, to enhance the tracking precision of the current controllers, the advance control techniques can be employed for the current loops. Due to the complexity of control technique in real time implementation, the PI controllers can be a good choice to guarantee the high tracking precision of the current loops. The simple diagram of current loops is shown in Fig. 4. The design of current controller is based on the PI controllers, which are shown in Fig. 4.

The output of PI current controller is $u_{\rm d}$ and $u_{\rm q}$ voltages. The design of the PI controller can be illustrated as

$$u_{dq} = K_P e_{dq} + \int K_i e_{dq} \tag{24}$$

where k_p and k_i are the proportional and integral gains, respectively, and e_{dq} is the error between reference and actual values of *d*- and *q*-axis currents. The e_{dq} can be expressed as

$$e_{dq} = i_{dq}^* - i_{dq} \tag{25}$$

where i_{dq}^* and i_{dq} are the reference and actual values for the current controllers, respectively.

VI. Antidisturbance Sliding Mode Speed Controller Based on the Proposed ATSMRL

A. Extended Sliding Mode Disturbance Observer (ESMDO)

In order to improve the control performance of the PMSM against lumped disturbances, the ESMDO has been designed to estimate the lumped disturbances *D(t)* online, then the estimated *D(t)* is carried out for the feed-forward compensation with i_q^*.

The ESMDO design is based on the conventional load torque observer, and its block diagram is shown in Fig. 5.

According to the load torque observer, the speed ω and *D(t)* are chosen as the state variables, the electromagnetic torque T_e

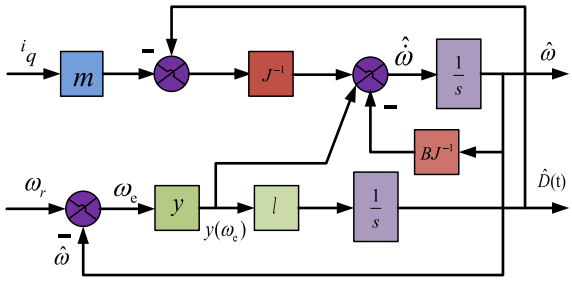

Fig. 5. Block diagram of the ESMDO.

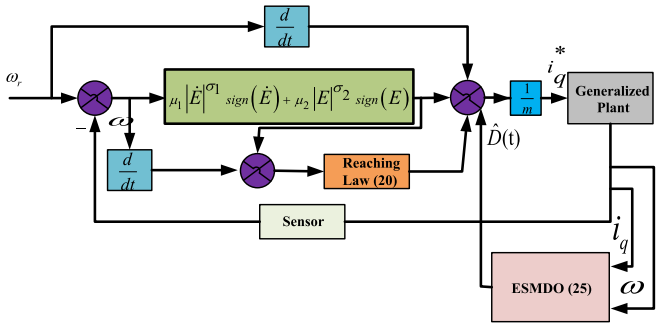

Fig. 6. Block diagram of ESMDO based ATSMRL for the speed regulation of PMSM.

is used as input of the system, and the speed is taken as the output of the system. The ESMDO equations can be expressed in state space as

$$\begin{bmatrix} \dot{\omega} \\ \dot{D}(t) \end{bmatrix} = \begin{bmatrix} -\frac{B}{J} & -\frac{1}{J} \\ 0 & 0 \end{bmatrix} \begin{bmatrix} \omega_r \\ D(t) \end{bmatrix} + \begin{bmatrix} \frac{1}{J} \\ 0 \end{bmatrix} T_e. \tag{26}$$

The motor speed and estimated disturbances are the observation objects, and then the sliding mode based disturbances can be obtained for (26), which can be written as

$$\begin{bmatrix} \dot{\widehat{\omega}} \\ \dot{\widehat{D}}(t) \end{bmatrix} = \begin{bmatrix} -\frac{B}{J} & -\frac{1}{J} \\ 0 & 0 \end{bmatrix} \begin{bmatrix} \widehat{\omega}_r \\ \widehat{D}(t) \end{bmatrix} + \begin{bmatrix} \frac{1}{J} \\ 0 \end{bmatrix} T_e - \begin{bmatrix} 1 \\ l \end{bmatrix} y(\omega_e) \tag{27}$$

where $y(\omega_e)$ is the sliding mode rate of the ESMDO observer for the speed error, and l is the observer gain. By combining (26) and (27), the observer error can be expressed as

$$\begin{cases} \dot{e}_\omega = -\frac{B}{J} e_\omega - \frac{1}{J} e_D \; y(\omega_e) \\ \dot{e}_D = -l y(\omega_e) \end{cases} \tag{28}$$

where e_ω and e_D are the speed and disturbance errors, respectively. The integral sliding mode surface is selected for the ESMDO, which can be described as

$$s_\omega = e_\omega + \int c e_\omega dt \tag{29}$$

by taking the derivative of (29), and the reaching law for ESMDO is

$$\dot{s}_\omega = \dot{e}_\omega + c e_\omega. \tag{30}$$

Thereof, the reaching law can be chosen as

$$\dot{s}_\omega = -k \; \text{sign}(s_\omega) \tag{31}$$

where k is the switching gain of the reaching law. By combining (30), (31) and using $-\frac{1}{J} e_D$ as the disturbances term, then the control law for ESMDO can be written as

$$y(\omega_e) = \left(c_\omega - \frac{B}{J} \right) e_\omega + k sign(s_\omega). \tag{32}$$

Equation (32) is the control law under the action of this SMC, then the state of the system would reach on the sliding mode surface in the finite time.

B. Stability Analysis of the ESMDO Observer

The Lyapunov function is selected to check the stability of the ESMDO. Therefore, the Lyapunov stability function can be described as

$$\lim_{s \to 0} \dot{V} = \lim_{s \to 0} s\dot{s} \le 0 \tag{33}$$

$$\begin{aligned} \dot{V} &= s_\omega \dot{s}_\omega = s_\omega \left[c e_\omega + \dot{e}_\omega \right] \\ &= s_\omega \left[c e_\omega + -\frac{B}{J} e_\omega + \frac{1}{J} e_D y(\omega_e) \right] \\ &= s_\omega \left[-k \; \text{sign}(s_\omega) \right] \\ &= -k \left| s_\omega \right| \le 0. \end{aligned} \tag{34}$$

Equation (34) has a coefficient k, which is a positive constant gain. The coefficient k would ensure that the designed ESMDO can get stable in terms of the tracking error, and converge to zero in the finite time.

C. Anti-disturbance Sliding Mode Speed Controller Based on the ATSMRL

The ESMDO can estimate the disturbances $\hat{D}(t)$ of the system, which can be compensated with the output of the speed controller. Then, the final output of the speed controller with disturbances compensation technique can be rewritten as

$$\begin{aligned} i_q^* = m_t{}^{-1} [& \dot{\omega}^* + \mu_1 \left| \dot{E} \right|^{\sigma_1} \text{sign} \left(\dot{E} \right) + \mu_2 |E|^{\sigma_2} \text{sign} \left(E \right) \\ & + \int_0^t -\bar{\Omega} \; \text{sign} \left\{ s + \frac{\dot{s} \left| \dot{s} \right|}{2 \Omega_r} \right\} dt + \hat{D}(t)]. \end{aligned} \tag{35}$$

The final antidisturbance block diagram of the CFTSMC based on both ATSMRL and ESMDO is shown in Fig. 6.

V. Experimental Validation

In order to verify the proposed method, the comprehensive experiments have been conducted in this section to demonstrate the speed and q-axis current performances of the PMSM from four typical cases, including start-up process, loading process, speed reversal process, and parametric mismatch.

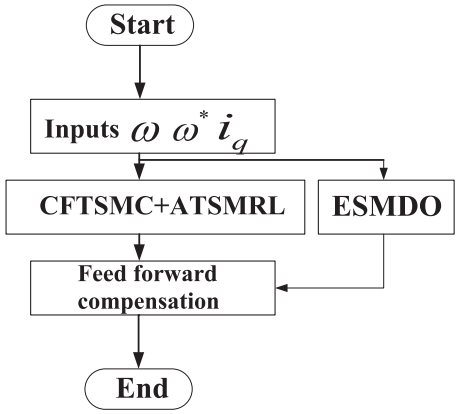

Fig. 7. Flowchart of the proposed (CFTSMC+ATSMRL) method with ESMDO.

TABLE I
PARAMETERS OF THE PMSM

Symbol	Name	Value and Unit
n_p	Machine pole pairs	3
p	Rated power	3.0 kW
n	Rated speed	2000 rpm
R_s	Stator resistance	0.8 Ω
ψ_f	Rotor flux linkage	0.35 Wb
L_s	dq-axis inductances	0.005 H
J	Inertia	$3.78\times10^{-4}\,kg.m^2$
B	Viscous damping	$1.74\times10^{-5}\,\mathrm{N}\cdot m\cdot s$ / rad

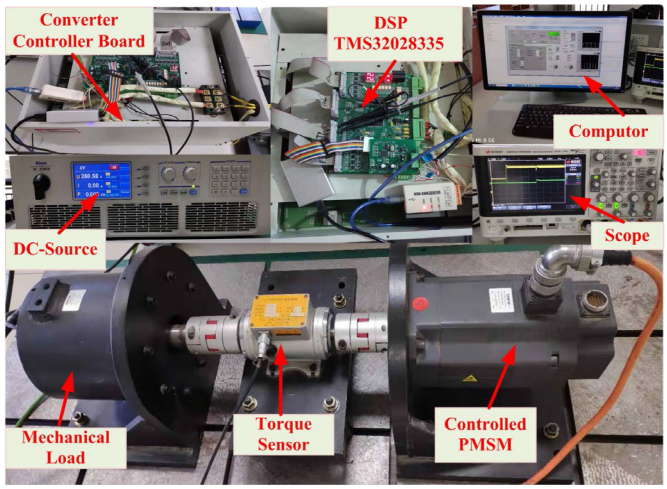

Fig. 8. Test platform.

The flowchart of the proposed method is shown in Fig. 7 and main parameters of the PMSM are given in Table I. To validate the effectiveness of the proposed method, one experimental test platform has been established, as depicted in Fig. 8. In addition, Fig. 9 shows the circuit diagram of the test platform. One three-phase rectifier is implemented to provide the dc power. The pulsewidth modulation (PWM) converter is adopted to drive

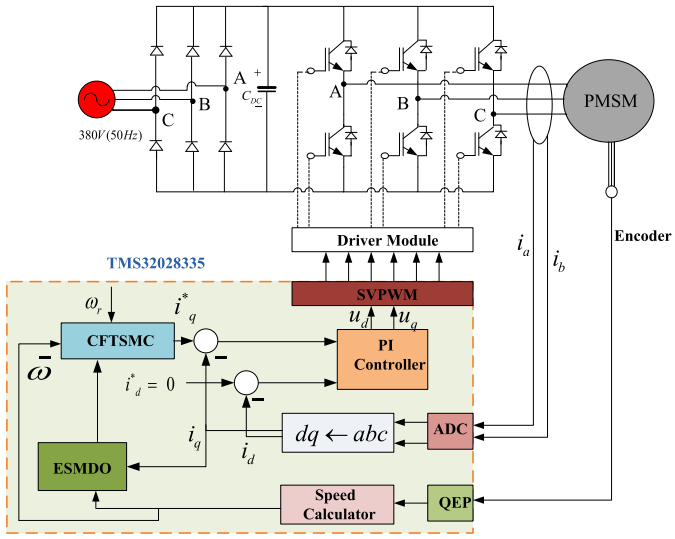

Fig. 9. Circuit diagram.

the system. Both 1 and 10 kHz sampling frequencies have been selected for the speed and current loops, respectively.

The full algorithm includes the space vector pulsewidth modulation (SVPWM), and DSP (TMS32028335) controller. The DSP code of the proposed method has been written in code composer studio (CCS) and then loaded to the DSP controller. The smart code (AU6802N1) sensor has been used, which has the characteristics of wide operating range in terms of temperature, including working temperature −40 °C to +125 °C, tracking rate 240,000/min, 20-MHz input clock, and 10 Bit resolution.

The Rohde and Schwarz, RTE-1024 scope, is selected to get the correct experimental results. The digital scope has sampling frequency band width of 200 MHz and 5G/s, respectively. The scope has four channels (MSO-X 3024A, and SSO-X3024A). The N2863B probes are selected to collect the results from the DSP, in which the probes rating are 10 MΩ, 15 pF, the attenuation ratio 10:1, 300 Vrms, and 300 MHz bandwidth. The control parameters of the PI, TSMR, and ATSMRL are optimized for the speed and current controllers, as listed in Table II.

A. Start-Up Response

The start-up speed performance of the PMSM under different control schemes are compared in details. The speed and q-axis current responses under the PI, ESMRL, TSMRL, ATSMRL, and ESMDO based ATSMRL during the start-up transient process are shown in Fig. 10(a) and (b), separately. As seen from Fig. 10(a), it is known that the PI controller has 16.5% overshoot, while the ESMRL [22], TSMRL [24], ATSMR, and ESMDO based ATSMRL have no overshoot at the start-up transient time. The settling process of the speed response under PI, ESMRL, TSMRL, ATSMRL, and ESMDO based ATSMRL is 0.234, 0.188, 0.089, 0.055, and 0.045 s, respectively.

It can be concluded that the start-up transient process of the speed response under the proposed ATSMRL is 76.5%, 62%, and 20% faster than those of the PI, ESMRL, and TSMRL, respectively. Moreover, Fig. 10(b) shows q-axis current response of

TABLE II
PARAMETERS OF THE CONTROL METHODS

Name	Value
PI gains of speed controller	120 and 50
PI gains of current controller	50 and 25
PI gains of current controller (SMC)	1 and 1000
Saturation limit	10 A
Sampling frequency of speed loop	1 kHz
Sampling frequency of current loop	10 kHz
The gains of TSMRL	μ_1=1000, μ_2=4000, k_1=0.001 and k_2=80000
The gains of ATSMRL	μ_1=1000, μ_2=4000, k_1=0.001 and k_2=80000, $\eta_1 = 20$ $\eta_2 = 3$ and $\Omega_r = 50$
The gains of ATSMRL+ESMDO	μ_1=1000, μ_2=4000 , k_1=0.001 and k_2 =80000, $\eta_1 = 20$ $\eta_2 = 3$ and $\Omega_r = 50$ c=30, l=0.001and k=5000.

TABLE III
COMPARISON OF START-UP TRANSIENT PERFORMANCE OF THE PI, TSMRL, ATSMRL, AND ESMDO BASED ATSMRL METHODS

Control Method	IAE Index of Speed Error Response	Settling Time (s)
PI	71746	0.234
ESMRL [22]	62832	0.188
TSMRL [24]	42807	0.089
ATSMRL	33967	0.055
ATSMRL+ESMDO	31980	0.045

the PMSM under PI, ESMRL, TSMRL, ATSMRL, and ESMDO based ATSMRL during the start-up transient process. Fig. 10(b) shows that the chattering phenomenon and current ripple in q-axis current under ATSMRL and ESMDO based ATSMRL are smaller than those of PI, ESMRL and TSMRL, respectively. It is evident from Fig. 10(b) that the q-axis current can approach to the steady state position under the PI, ESMRL, TSMRL, ATSMRL, and ESMDO based ATSMRL in 0.234, 0.188, 0.089, 0.055, and 0.045 s, respectively.

Furthermore, the integral absolute error (IAE) is chosen to calculate the speed responses during steady state process under the PI, ESMRL, TSMRL, ATSMRL, and ESMDO based ATSMRL, separately. The IAE can be expressed as

$$\omega = \frac{\sqrt{\frac{1}{N}\sum_{i=1}^{N}(\omega_m(i) - \omega_{av})^2}}{\omega_{av}} \tag{36}$$

where $\omega_m(i)$ and ω_{av} are the instantaneous and average speed value, respectively. The IAE index of the speed responses is calculated during the start-up process, as listed in Table III.

Furthermore, Fig. 11 shows the speed and q-axis current responses under TSMRL, ATSMRL, and ESMDO based ATSMRL at the reference speed of 2000 rpm, separately.

It is obviously shown in Fig. 11(a) that the steady state error of the speed response under TSMRL is more than those of ATSMRL and ESMDO based ATSMRL. The q-axis current responses under TSMR, ATSMRL, and ESMDO based ATSMRL are compared with each other. In Fig. 11(b), it is known that the

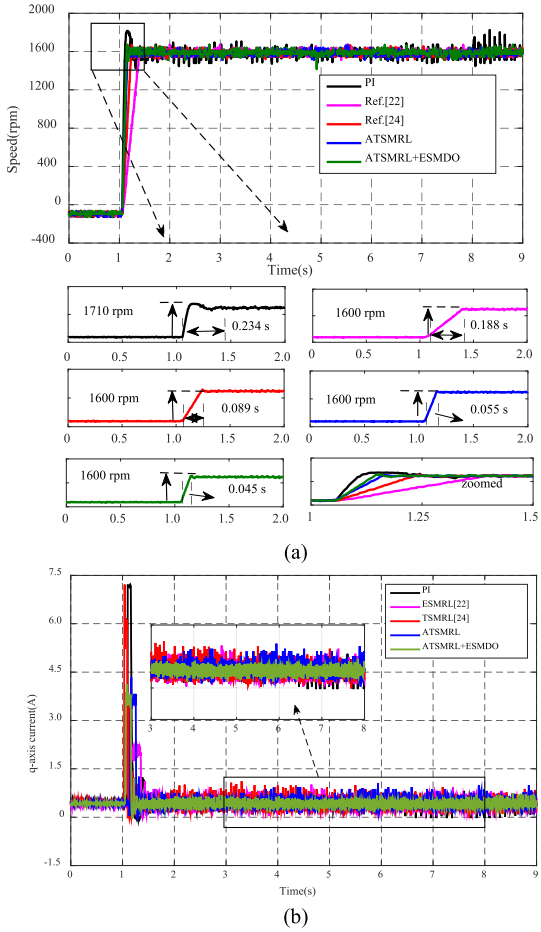

Fig. 10. Speed and q-axis current responses under PI, ESMRL, TSMRL, ATSMRL, and ESMDO based ATSMRL controller with the no-load @ 1600 r/min. (a) Speed. (b) q-axis current.

ESMDO based ATSMRL, and ATSMRL have smaller chattering and current ripples than those of the TSMRL.

B. Load Adding Response

The speed performance of the PMSM under the PI, ESMRL, TSMRL, ATSMRL, and ESMDO based ATSMRL is compared under the loading condition. The speed and q-axis current responses are taken with the load of 5 Nm at the reference speed of 1200 rpm. The speed and q-axis current responses under the PI, ESMRL, TSMRL, ATSMRL, and ESMDO based ATSMRL are shown in Fig. 12, respectively. As shown in Fig. 12(a), the settling times of the speed response under the PI, ESMRL, TSMRL, ATSMRL, and ESMDO based ATSMRL are 0.245, 0.125, 0.112, 0.083, and 0.070s respectively. Also, it is shown that the speed drop under the PI, ESMRL, TSMRL, ATSMRL and ESMDO based ATSMRL is 332, 317, 308, 289, and 265 rpm, respectively.

Fig. 12(b) shows the q-axis current responses under the controls of PI, ESMRL, TSMRL, ATSMRL, and ESMDO based ATSMRL at 1200 rpm with 5 Nm load. It is known that the

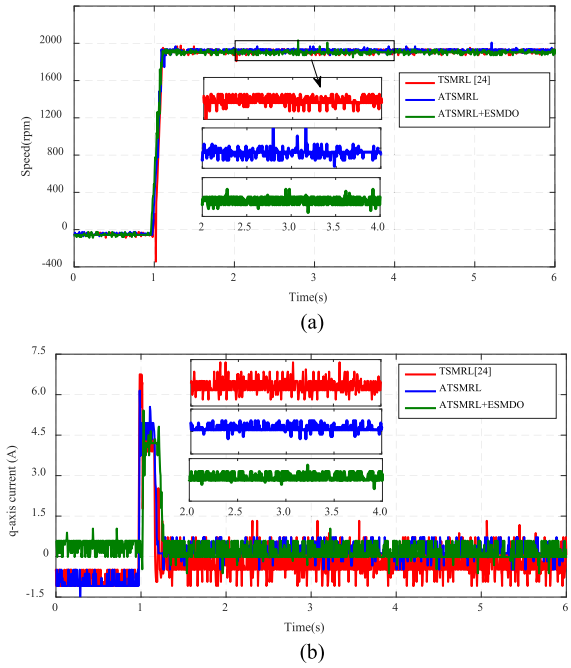

Fig. 11. Speed and q-axis current responses under TSMRL, ATSMRL and ESMDO based ATSMRL controller with the no load @ 2000 r/min. (a) Speed. (b) q-axis current.

TABLE IV
TRANSIENT PERFORMANCE COMPARISON OF PI, TSMRL, ATSMRL, AND ESMDO BASED ATSMRL METHODS

Control Method	IAE Index of Speed Error Response	Settling Time at Load (s)	Speed Drop (rpm)
PI	63467	0.7	445
TSMRL	51578	0.64	490
ATSMRL	32467	0.61	425
ATSMRL+ESMDO	27680	0.4	390

ESMDO based ATSMRL has the quickest q-axis current response in terms of current ripple and chattering among these five methods.

Furthermore, the speed and q-axis current responses are taken with the load of 10 Nm at the reference speed of 1600 and 2000 rpm, respectively. The speed and q-axis current responses under PI, TSMRL, ATSMRL, and ESMDO based ATSMRL are shown in Figs. 13 and 14, respectively. It is seen from Fig. 13 that the PI controller has an overshoot, while TSMRL, ATSMRL, and ESMDO based ATSMRL have no overshoot at start-up process, respectively. The settling transient process of the speed response at loading point under PI, TSMRL, ATSMRL, and ESMDO based ATSMRL is 0.7, 0.64, 0.61, and 0.4 s, separately. Furthermore, as seen from this figure, the speed drop under PI, TSMRL, ATSMRL, and ESMDO based ATSMRL is 445, 490, 425, and 390 rpm, respectively.

Moreover, the IAE index of PI, TSMRL, ATSMRL, and ESMDO based ATSMRL, is listed in Table IV, respectively.

In addition, Fig. 14 shows the q-axis current responses of the PMSM under PI, TSMRL, ATSMRL, and ESMDO based ATSMRL during the loading condition. It is evident from Fig. 14

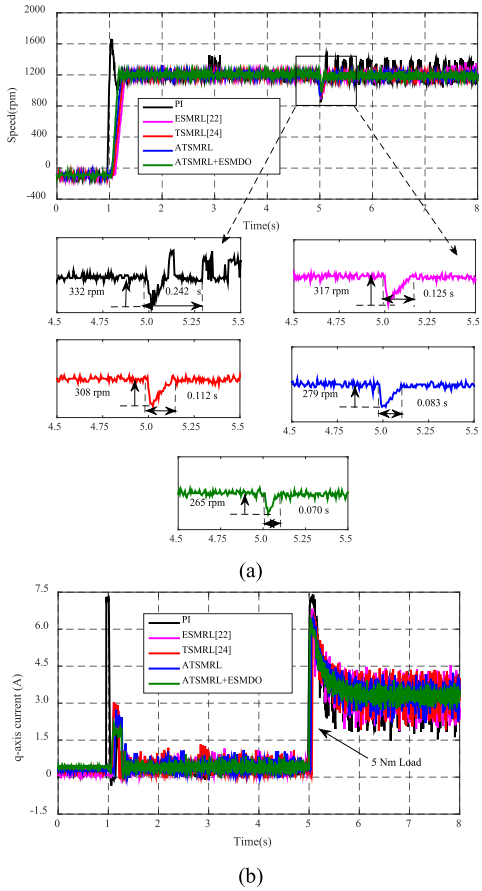

Fig. 12. Speed and q-axis current responses under PI, ESMRL, TSMRL, ATSMRL and ESMDO based ATSMRL controller with the load @ 1200 r/min. (a) Speed. (b) q-axis current.

that both PI and TSMRL have bigger current ripple and chattering than those of ATSMRL, and ESMDO based ATSMRL, respectively.

Moreover, the speed and q-axis current responses are taken at the reference speed of 2000 rpm with the load of 10 Nm. The speed and q-axis current responses under PI, TSMRL, ATSMRL, and ESMDO based ATSMRL are shown in Fig. 15. It is shown in Fig. 15(a) that the speed drop under TSMR, ATSMRL, and ESMDO based ATSMRL with 10 Nm load is 300, 250, and 150 rpm, respectively. Moreover, as seen from this figure, the speed fluctuation in TSMRL is higher than those of ATSMRL, and ESMDO based ATSMRL.

Fig. 15(b) shows the q-axis current responses of the PMSM under TSMRL, ATSMRL, and ESMDO based ATSMRL with 10 Nm loading condition, respectively. It is evident from Fig. 15(b) that TSMRL has higher current ripple and chattering than those of ATSMRL, and ESMDO based ATSMRL, respectively.

C. Speed Reversal Response

The speed reversal and steady state performance of the PMSM under PI, TSMRL, ATSMRL, and ATSMRL with ESMDO are fully compared. The speed and q-axis current responses for PI,

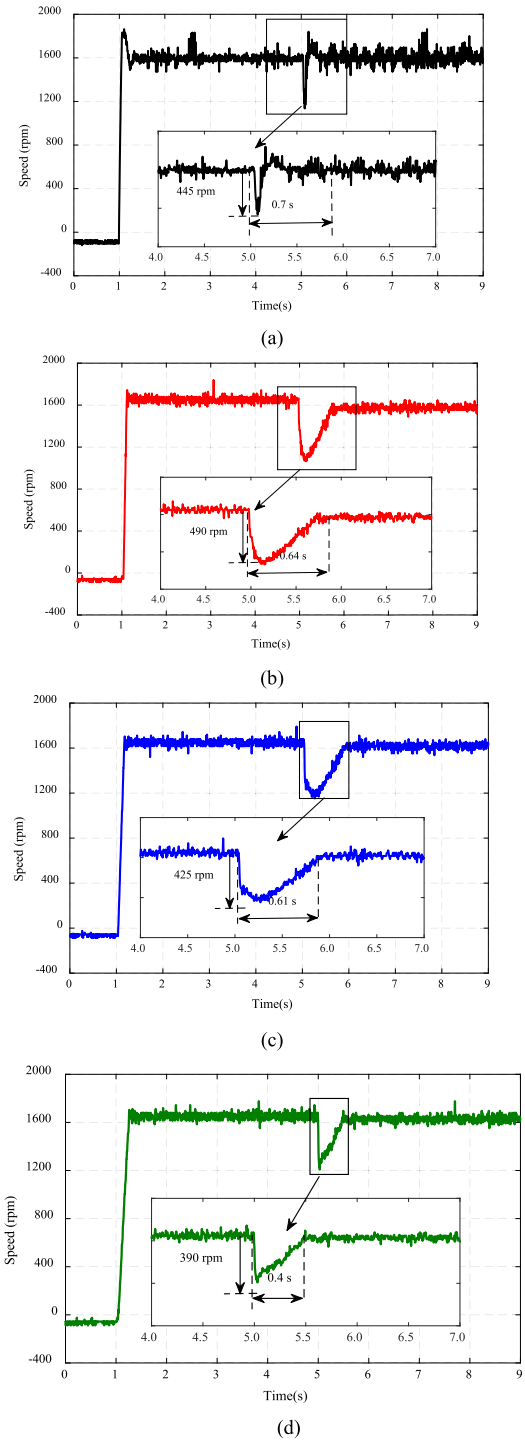

Fig. 13. Speed responses under the load of 10 Nm @ 1600 r/min. (a) PI. (b) TSMRL. (c) ATSMRL. (d) ESMDO.

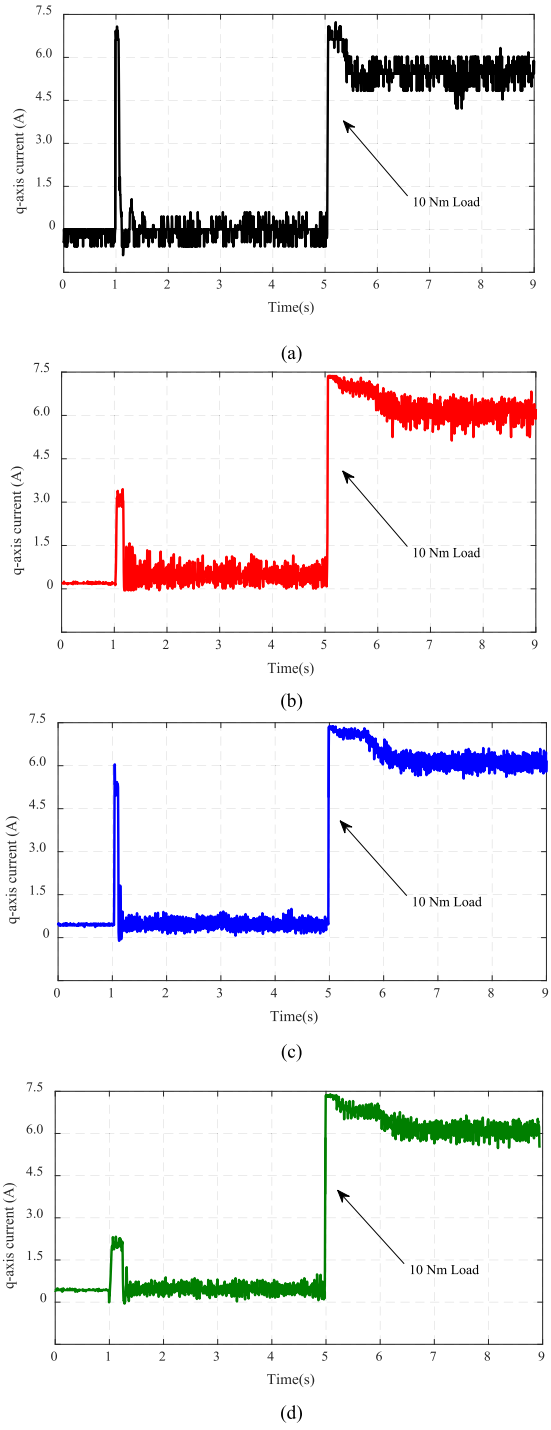

Fig. 14. q-axis current responses under the load of 10 Nm @ 1600 r/min. (a) PI. (b) TSMRL. (c) ATSMRL. (d) ESMDO.

TSMRL, ATSMRL, and ATSMRL based ESMDO during the speed reversal transient, from 2000 to -2000 rpm and then back to 2000 rpm, are shown in Fig. 16.

It is evident from Fig. 16(a) that the speed under PI has an overshoot with more settling time than those of TSMRL, ATSMRL and ATSMRL based ESMDO, when their speed changes from 2000 to -2000 rpm and then back to 2000 rpm. At the same time, it can be noted that the steady state error of the speed in PI and TSMRL are higher than those of ATSMRL and ESMDO based ATSMRL, respectively. Furthermore, the q-axis current responses are taken under speed reversal process. It is seen from Fig. 16(b) that the q-axis current ripple and chattering under PI and TSMRL are bigger than those of ATSMRL and ESMDO based ATSMRL.

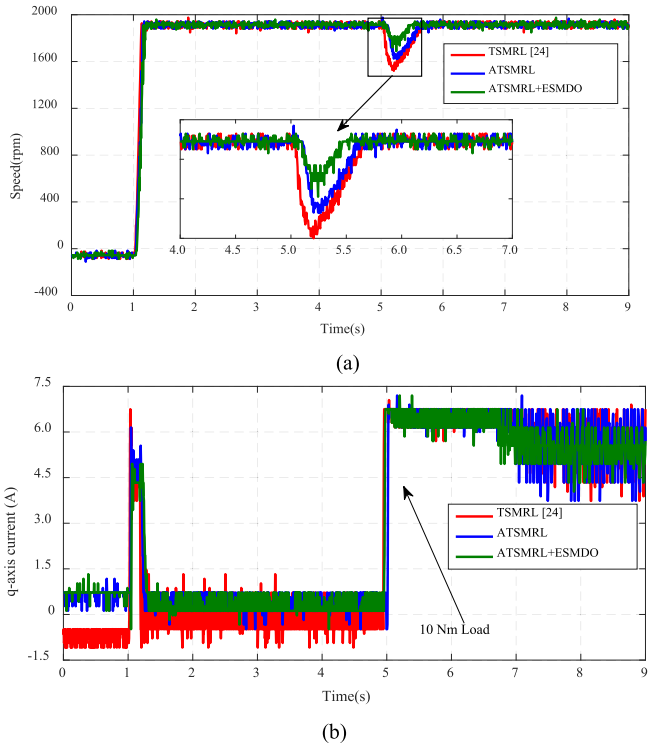

Fig. 15. Speed and q-axis current responses under TSMRL, ATSMRL, and ESMDO based ATSMRL controller with the load of 10 Nm @ 2000 r/min. (a) Speed. (b) q-axis current.

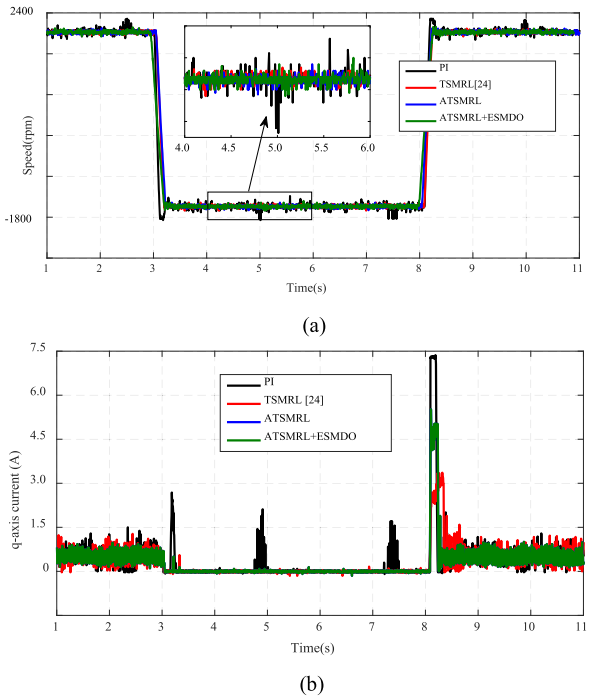

Fig. 16. Speed and q-axis current responses under PI, TSMRL, ATSMRL, and ESMDO based ATSMRL controller with the speed reversal @ 2000 r/min. (a) Speed. (b) q-axis current.

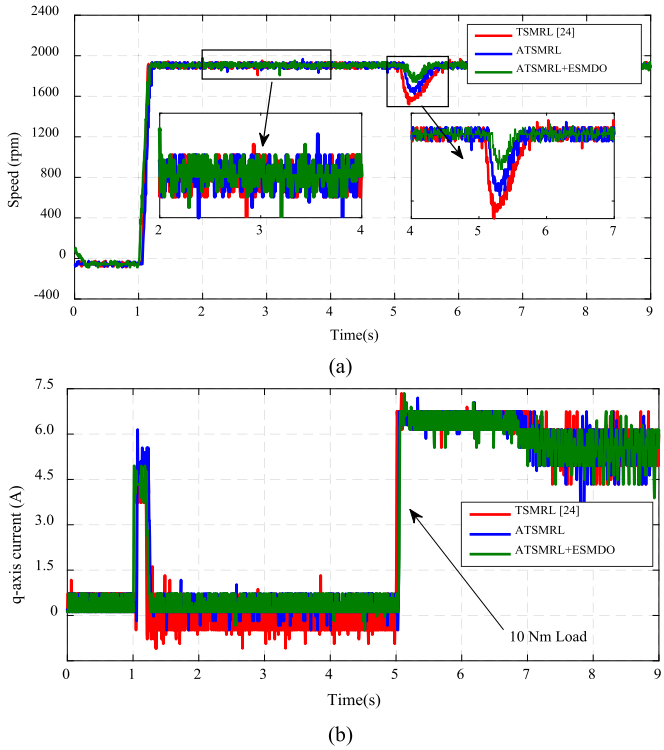

Fig. 17. Speed and q-axis current responses under TSMRL, ATSMRL, and ESMDO based ATSMRL controller at half inertia (0.5J) mismatch with the load of 10 Nm @ 2000 r/min. (a) Speed. (b) q-axis current.

D. Speed Response Under Parameters Change

In this article, the speed loop is considered that is why the resistance and inductance mismatch can be omitted. The speed performance under inertia mismatch is sufficient to check the robustness of the PMSM for speed regulation. The speed and q-axis current performance under the inertia mismatch are fully compared. The speed and q-axis current responses under TSMRL, ATSMRL, and ESMDO based ATSMRL with half and double (0.5 J and 2 J) inertia mismatch under the load of 10 Nm are shown in Figs. 17 and 18, separately.

It is noted from Fig. 17(a) that the steady state error of the speed response in TSMRL is bigger than those of the ATSMRL, and ESMDO based ATSMRL, respectively. Furthermore, as seen from this figure, the speed drop under TSMRL, ATSMRL, and ESMDO based ATSMRL is 248, 215, and 160 rpm, separately.

Fig. 17(b) shows the q-axis current response under the TSMRL, ATSMRL, and ESMDO based ATSMRL with load of 10 Nm, respectively. It is evident from Fig. 17(b) that the TSMRL has higher current ripple and chattering than those of the ATSMRL, and ESMDO based ATSMRL under half inertia (0.5J) mismatch, separately.

Furthermore, it is evident from Fig. 18(a) that the steady state error of the speed response in the TSMRL is higher than those of the ATSMRL, and ESMDO based ATSMRL, respectively. Moreover, as seen from this figure, the speeds drop under the

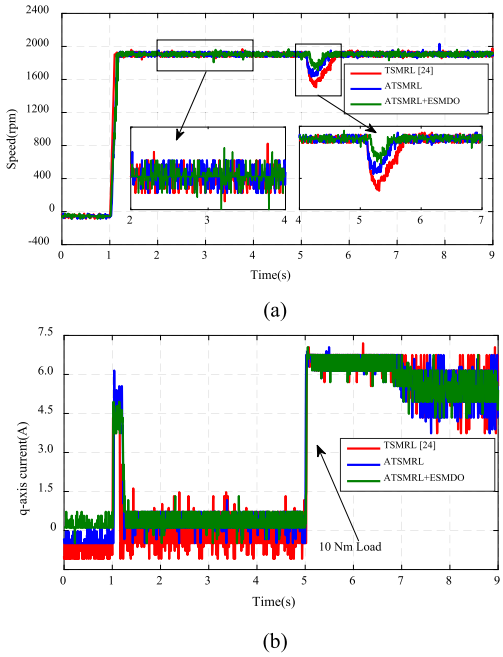

Fig. 18. Speed and q-axis current responses under the TSMRL, ATSMRL, and ESMDO based ATSMRL controller at double inertia ($2J$) mismatch with the load of 10 Nm @ 2000 r/min. (a) Speed. (b) q-axis current.

TSMRL, ATSMRL, and ESMDO based ATSMRL is 254, 186, and 158 rpm, respectively.

Meanwhile, Fig. 18(b) shows the q-axis current response under the TSMRL, ATSMRL, and ESMDO based ATSMRL with load of 10 Nm, respectively. It is evident from Fig. 18(b) that the TSMRL has higher current ripple and chattering than those of the ATSMRL, and ESMDO based ATSMRL under double inertia (2J) mismatch.

VI. Conclusion

In this article, a new adaptive reaching law (ATSMRL) has been proposed to improve the dynamic performance of the PMSM drive system. The ATSMRL is used to improve the reaching velocity under starting and load transient, and suppress the chattering phenomena effectively, which is different from those of the ESMRL [22] and TSMRL [24], respectively.

Then, considering the chattering phenomena caused by the switching high gains, an ESMDO has been developed to estimate the total system disturbances for the feed-forward compensation technique.

In order to further strengthen the disturbance rejection ability and eliminate the chattering phenomena, one improved ESMDO combining both CFTSMC and ATSMRL is presented in this work. The stability of close loop control system combined with ESMDO is presented and verified by Lyapunov function. Detailed comparisons have been fully made on the robust ability against load disturbance and parametric mismatch among five methods, including the proposed ATSMRL in this article, conventional PI, the existing ESMRL [22], the existing TSMRL [24], and proposed ATSMRL based ESMDO methods. Comprehensive numerical analysis and experiments have demonstrated the proposed ATSMR can benefit from the faster transient response, quicker reduction of chattering, and stronger disturbance rejection ability over the existing methods.

References

[1] W. Xu, A. K. Junejo, Y. Liu, and M. R. Islam, "Improved continuous fast terminal sliding mode control with extended state observer for speed regulation of PMSM drive system," *IEEE Trans. Veh. Technol.*, vol. 68, no. 11, pp. 10465–10476, Jul. 2019.

[2] X. Zhang, L. Sun, K. Zhao, and L. Sun, "Nonlinear speed control for PMSM system using sliding-mode control and disturbance compensation techniques," *IEEE Trans. Power Electron.*, vol. 28, no. 3, pp. 1358–1365, Mar. 2013.

[3] F. Mwasilu and J. Jung, "Enhanced fault-tolerant control of interior PMSMs based on an adaptive EKF for EV traction applications," *IEEE Trans. Power Electron.*, vol. 31, no. 8, pp. 5746–5758, Aug. 2016.

[4] G. Du, W. Xu, J. Zhu, and N. Huang, "Effects of design parameters on the multiphysics performance of high-speed permanent magnet machines," *IEEE Trans. Ind. Electron.*, vol. 67, no. 5, pp. 3472–3483, May. 2020.

[5] X. Li, W. Xu, C. Ye, and I. Boldea, "Comparative study of transversal-flux permanent magnetic linear oscillatory machines for compressor," *IEEE Trans. Ind. Electron.*, vol. 65, no. 9, pp. 7437–7446, Sep. 2018.

[6] A. H. Almarhoon, Z. Q. Zhu, and P. L. Xu, "Improved pulsating signal injection using zero-sequence carrier voltage for sensorless control of dual three-phase PMSM," *IEEE Trans. Energy Convers.*, vol. 32, no. 2, pp. 436–446, Jun. 2017.

[7] H. Du, X. Chen, G. Wen, X. Yu, and J. Lü, "Discrete-time fast terminal sliding mode control for permanent magnet linear motor," *IEEE Trans. Ind. Electron.*, vol. 65, no. 12, pp. 9916–9927, Dec. 2018.

[8] W. Xu, J. Zou, and C. Mu, "Improved model predictive current control strategy-based rotor flux for linear induction machines," *IEEE Trans. Appl. Supercond.*, vol. 26, no. 7, pp. 1–5, Oct. 2016.

[9] Y. Feng, X. Yu, and F. Han, "High-order terminal sliding-mode observer for parameter estimation of a permanent-magnet synchronous motor," *IEEE Trans. Ind. Electron.*, vol. 60, no. 10, pp. 4272–4280, Oct. 2013.

[10] C. Mu and H. He, "Dynamic behavior of terminal sliding mode control," *IEEE Trans. Ind. Electron.*, vol. 65, no. 4, pp. 3480–3490, Apr. 2018.

[11] S. S. Xu, C. Chen, and Z. Wu, "Study of nonsingular fast terminal sliding-mode fault-tolerant control," *IEEE Trans. Ind. Electron.*, vol. 62, no. 6, pp. 3906–3913, Jun. 2015.

[12] A. K. Junejo, W. Xu, C. Mu, and Y. Liu, "Improved fast terminal sliding mode control for speed regulation of surface-mounted permanent magnet synchronous motor," in *Proc. Inter. Conf. Elect. Mach. Syst.*, Oct. 2018, pp. 93–98.

[13] D. Liang, J. Li, R. Qu, and W. Kong, "adaptive second-order sliding-mode observer for PMSM sensorless control considering VSI nonlinearity," *IEEE Trans. Power Electron.*, vol. 33, no. 10, pp. 8994–9004, Oct. 2018.

[14] M. Cheema, J. Fletcher, M. Farshadnia, and M. Rahman, "Sliding mode based combined speed and direct thrust force control of linear permanent magnet synchronous motors with first-order plus integral sliding condition," *IEEE Trans. Power Electron.*, vol. 34, no. 3, pp. 2526–2538, Mar. 2019.

[15] X. Wang, M. Reitz, and E. Yaz, "Field oriented sliding mode control of surface-mounted permanent magnet AC motors: Theory and applications to electrified vehicles," *IEEE Trans. Veh. Technol.*, vol. 67, no. 11, pp. 10343–10356, Nov. 2018.

[16] A. Saghafinia, H. Ping, M. Uddin, and K. Gaeid, "Adaptive fuzzy sliding-mode control into chattering-free IM drive," *IEEE Trans. Ind Appl.*, vol. 51, no. 1, pp. 692–701, Jan./Feb. 2015.

[17] R. Jan, C. Tseng, and R. Liu, "Robust PID control design for permanent-magnet synchronous motor: A genetic approach," *Electric Power Syst. Res.*, vol. 78, no. 7, pp. 1161–1168, Jul. 2008.

[18] K. Han, M. Choi, B. Lee, and S. B. Choi, "Development of a traction control system using a special type of sliding mode controller for hybrid 4WD vehicles," *IEEE Trans. Veh. Technol.*, vol. 67, no. 1, pp. 264–274, Jan. 2018.

[19] W. Xu, Y. Jiang, C. Mu, and F. Blaabjerg, "Improved nonlinear flux observer-based second-order SOIFO for PMSM sensorless control," *IEEE Trans. Power Electron.*, vol. 34, no. 1, pp. 565–579, Jan. 2019.

[20] M. Do, Z. Man, C. Zhang, H. Wang, and F. S. Tay, "Robust sliding mode-based learning control for steer-by-wire systems in modern vehicles," *IEEE Trans. Veh. Technol.*, vol. 63, no. 2, pp. 580–590, Feb. 2014.
[21] C. Fallaha, M. Saad, H. Y. Kanaan, and K. Al-Haddad, "Sliding-mode robot control with exponential reaching law," *IEEE Trans. Ind. Electron.*, vol. 58, no. 2, pp. 600–610, Feb. 2011.
[22] W. Gao and J. C. Hung, "Variable structure control of nonlinear systems: A new approach," *IEEE Trans. Ind. Electron.*, vol. 40, no. 1, pp. 45–55, Feb. 1993.
[23] H. Ma, J. Wu and Z. Xiong, "A novel exponential reaching law of discrete-time sliding-mode control," *IEEE Trans. Ind. Electron.*, vol. 64, no. 5, pp. 3840–3850, May 2017.
[24] H. Wang *et al.*, "Continuous fast nonsingular terminal sliding mode control of automotive electronic throttle systems using finite-time exact observer," *IEEE Trans. Ind. Electron.*, vol. 65, no. 9, pp. 7160–7172, Sep. 2018.
[25] Q. Xu, "Piezoelectric nanopositioning control using second-order discrete-time terminal sliding-mode strategy," *IEEE Trans. Ind. Electron.*, vol. 62, no. 12, pp. 7738–7748, Dec. 2015.
[26] J. Lara, J. Xu, and A. Chandra, "Effects of rotor position error in the performance of field-oriented-controlled PMSM drives for electric vehicle traction applications," *IEEE Trans. Ind. Electron.*, vol. 63, no. 8, pp. 4738–4751, Aug. 2016.
[27] F. Fateh, W. N. White, and D. Gruenbacher, "Torsional vibrations mitigation in the drivetrain of DFIG-based grid-connected wind turbine," *IEEE Trans. Ind App.*, vol. 53, no. 6, pp. 5760–5767, Dec. 2017.

Abdul Khalique Junejo was born in Larkana, Sindh province, Pakistan, in 1989. He received the bachelor's and master's degrees in electrical engineering from Quaid-e-Awam UEST Nawabshah, Sindh Pakistan, in 2011 and 2015, respectively. He is currently working towards Ph.D. degree with the School of electrical and electronics engineering with the State Key Laboratory of advanced Electromagnetic Engineering, Huazhong university of Science and Technology, Wuhan, China.

He is currently employed an Assistant Professor in Quaid-e-Awam UEST Nawabshah, Sindh, Pakistan. His research interests include the sliding mode control, linear and nonlinear control methods for permanent magnet synchronous machines and drives.

Wei Xu (Senior Member, IEEE) received the B.E. and M.E. degrees from Tianjin University, Tianjin, China, in 2002 and 2005, and the Ph.D. degree from the Institute of Electrical Engineering, Chinese Academy of Sciences, in 2008, all in electrical engineering.

From 2008 to 2012, he was a Postdoctoral Fellow with University of Technology Sydney, and a Vice Chancellor Research Fellow with Royal Melbourne Institute of Technology, Japan Science Promotion Society Invitation Fellow with Meiji University. Since 2013, he has been a Full Professor with the State Key Laboratory of Advanced Electromagnetic Engineering with the Huazhong university of Science and Technology, China. He has authored more than 100 papers accepted or published in IEEE Transactions Journals, two edited books published by Springer Press, one monograph published by China Machine Press, and 120 invention patents granted or pending, all in the related fields of electrical machines and drives. His research topics mainly cover design and control of linear/rotary machines.

Mr. Xu is a fellow of the Institute of Engineering and Technology (IET). He has served as Associate Editor for several Journals, such as IEEE TRANSACTIONS ON INDUSTRIAL ELECTRONICS, and so on.

Chaoxu Mu (Senior Member, IEEE) received the Ph.D. degree in control science and engineering from the School of Automation, Southeast University, Nanjing, China, in 2012.

She was a Visiting Ph.D. Student with the Royal Melbourne Institute of Technology University, Melbourne, VIC, Australia, from 2010 to 2011. From 2014 to 2016, she was a Postdoctoral Fellow with the Department of Electrical, Computer and Biomedical Engineering, The University of Rhode Island, Kingston, RI, USA. She is currently a Professor with the School of Electrical and Information Engineering, Tianjin University, Tianjin, China. She has authored over 100 journal and conference papers, and coauthored two monographs. Her current research interests include nonlinear system control and optimization, adaptive and learning systems.

Moustafa Magdi Ismail received the B.Sc. and M.Sc. degrees from the School of Electrical Engineering, Minia University, EL-Minya, Egypt, in 2011 and 2016, respectively. He is currently working toward the Ph.D. degree with the State Key Laboratory of Advanced Electromagnetic Engineering and Technology, School of Electrical and Electronic Engineering, Huazhong University of Science and Technology, Wuhan, China.

He was appointed as an Assistant Lecturer in the School of Electrical Engineering, Minia University, from October 2011 to September 2017. His current research interests include advanced control of electrical drives, power converter systems, smart grids, and optimization algorithms.

Yi Liu (Member, IEEE) received the B.E. and M.E. degrees in automation and control engineering from the Wuhan University of Science and Technology, Wuhan, China, in 2004 and 2007, respectively, and the Ph.D. degree in mechatronic engineering from the Huazhong University of Science and Technology, Wuhan, in 2016.

From 2007 to 2011, he was a Lecturer at the City College, Wuhan University of Science and Technology. From March 2016 to June 2016, he was a Senior R&D Engineer at the Fourth Academy of China Aerospace Science and Industry Group, Wuhan. In July 2016, he became a Postdoctoral Research Fellow at the State Key Laboratory of Advanced Electromagnetic Engineering and Technology, School of Electrical and Electronic Engineering, Huazhong University of Science and Technology, where he has been a Lecturer since January 2020. His current research interests include multiport electrical machines and drive systems.